

High Order Semi-Lagrangian Discontinuous Galerkin Method Coupled with Runge-Kutta Exponential Integrators for Nonlinear Vlasov Dynamics

Xiaofeng Cai¹, Sebastiano Boscarino², Jing-Mei Qiu³

Abstract. In this paper, we propose a semi-Lagrangian discontinuous Galerkin method coupled with Runge-Kutta exponential integrators (SLDG-RKEI) for nonlinear Vlasov dynamics. The commutator-free Runge-Kutta (RK) exponential integrators (EI) were proposed by Celledoni, et al. (FGCS, 2003). In the nonlinear transport setting, the RKEI can be used to decompose the evolution of the nonlinear transport into a composition of a sequence of linearized dynamics. The resulting linearized transport equations can be solved by the semi-Lagrangian (SL) discontinuous Galerkin (DG) method proposed in Cai, et al. (JSC, 2017). The proposed method can achieve high order spatial accuracy via the SLDG framework, and high order temporal accuracy via the RK EI. Due to the SL nature, the proposed SLDG-RKEI method is not subject to the CFL condition, thus they have the potential in using larger time-stepping sizes than those in the Eulerian approach. Inheriting advantages from the SLDG method, the proposed SLDG-RKEI schemes are mass conservative, positivity-preserving, have no dimensional splitting error, perform well in resolving complex solution structures, and can be evolved with adaptive time stepping sizes. We show the performance of the SLDG-RKEI algorithm by classical test problems for the nonlinear Vlasov-Poisson system, as well as the Guiding center Vlasov model. Though that it is not our focus of this paper to explore the SLDG-RKEI scheme for nonlinear hyperbolic conservation laws that develop shocks, we show some preliminary results on schemes' performance on the Burgers' equation.

Key Words: Semi-Lagrangian; Discontinuous Galerkin; Runge-Kutta exponential integrators; Vlasov-Poisson; Guiding center Vlasov model; Mass conservative; Positivity-preserving; Adaptive time-stepping algorithm.

¹ Department of Mathematical Sciences, University of Delaware, Newark, DE, 19716. E-mail: xfcai@udel.edu.

² Department of Mathematics and Computer Science, University of Catania, Catania, 95127, E-mail: boscarino@dmf.unict.it.

³Corresponding Author. Department of Mathematical Sciences, University of Delaware, Newark, DE, 19716. E-mail: jingqiu@udel.edu. Research of first and last author is supported by NSF grant NSF-DMS-1818924, Air Force Office of Scientific Computing FA9550-18-1-0257 and University of Delaware.

1 Introduction

In this paper, we consider the following two nonlinear Vlasov models. The first is the nonlinear Vlasov-Poisson system

$$f_t + v f_x + E(x, t) f_v = 0, \quad (1.1)$$

$$E(x, t) = -\phi_x, \quad -\phi_{xx}(x, t) = \rho(x, t). \quad (1.2)$$

Here x and v are the coordinates in the phase space $(x, v) \in \Omega_x \times \mathbb{R}$; the electron distribution function $f(x, v, t)$ is the probability distribution function describing the probability of finding a particle with velocity v at position x and at time t . The electric field $E = -\phi_x$, where the self-consistent electrostatic potential ϕ is determined by Poisson's equation (1.2). $\rho(x, t) = \int_{\mathbb{R}} f(x, v, t) dv - 1$ denotes charge density, with the assumption that infinitely massive ions are uniformly distributed in the background. The second model is the guiding center Vlasov model which describes a highly magnetized plasma in the transverse plane of a tokamak [18, 10]:

$$\rho_t + \nabla \cdot (\mathbf{E}^\perp \rho) = 0, \quad (1.3)$$

$$-\Delta \Phi = \rho, \quad \mathbf{E}^\perp = (-\Phi_y, \Phi_x), \quad (1.4)$$

where the unknown variable ρ denotes the charge density of the plasma, and the electric field \mathbf{E} depends on ρ via the Poisson equation. Both models can be written in the form of

$$u_t + \nabla \cdot (\mathbf{P}(u; \mathbf{x}, t) u) = 0, \quad (\mathbf{x}, t) \in \mathbb{R}^d \times [0, T], \quad (1.5)$$

where $u : \mathbb{R}^d \times [0, T] \rightarrow \mathbb{R}$, $\mathbf{P}(u; \mathbf{x}, t) = (P_1(u; \mathbf{x}, t), \dots, P_d(u; \mathbf{x}, t))^T$ with $P_i : \mathbb{R} \times \mathbb{R}^d \times [0, T] \rightarrow \mathbb{R}$, $i = 1, \dots, d$ are velocity fields that are u -dependent for nonlinear dynamics.

Popular mesh-based approaches for the above mentioned nonlinear transport models are the Eulerian and semi-Lagrangian (SL) approaches. Eulerian methods are usually built by a spatial discretization coupled by a temporal time discretization of the partial differential equations via the method-of-lines approach; while SL methods are designed taking into account characteristics tracing. Despite the complication in building in the characteristics tracking mechanism, when properly designed, SL methods can circumvent the stringent CFL constraint in an Eulerian approach, thus achieve computational savings by taking larger time-stepping sizes. In particular, when performing a time integration of a system, one would take Δt to be $\min(\Delta t_{acc}, \Delta t_{stab})$, where Δt_{acc} stands

for the time stepping size from accuracy consideration, while Δt_{stab} is the time stepping size from stability consideration. By working with the SL approach, Δt_{stab} could be greatly relaxed, so that one can take the time stepping size with accuracy consideration only, leading to computational savings by taking a larger time stepping size.

The use of high order SL methods for nonlinear dynamic such as (1.5) presents the following two issues.

- One is the tracking of characteristics with high order temporal accuracy. Research efforts have been made to accurately track characteristics for nonlinear Vlasov dynamics [15]; yet the problem-dependent procedures become more and more complicated when higher order temporal accuracy is desired. On the other hand, a class of commutator-free Runge-Kutta (RK) exponential integrator (EI) are proposed in the context of SL schemes to solve the nonlinear convection-dominated problems [8]. The RKEI framework constructs schemes by decomposing the nonlinear dynamic process into a sequence of linearized linear solvers; and the high order temporal accuracy is achieved by matching order conditions. The RKEI schemes are represented in the form of Butcher tableaux; as such, the schemes can be implemented in a black-box manner, as in implementing the RK time discretization in an Eulerian approach.
- The second issue is the design of accurate SL spatial discretization with mass conservation. In this paper, we propose to apply the SLDG algorithm for linear transport problems [2] to couple with the RKEI for nonlinear Vlasov dynamics. While in principle different SL spatial discretizations could be applied in this context, e.g. see [6, 13, 7], we propose to use the multi-dimensional SLDG method for its mass conservation, high order spatial accuracy, compactness, positivity preserving (PP), and superconvergence properties for long-time integration.

The rest of this paper is organized as follows. In Section 2, we propose to couple the SLDG and RKEI method; in Section 3, the performance of the proposed method is shown through extensive numerical tests. Finally, concluding remarks are made in Section 4.

2 SLDG-RKEI schemes

In this section, we will present the proposed SLDG-RKEI method that combines the SLDG schemes [2] with the high order RKEI in [8] for solving nonlinear transport problems. We will first review the SLDG scheme for linear transport problems. To extend this SLDG solver for nonlinear transport problems, we start by illustrating a first order SLDG-RKEI scheme that updates the solution by using the SLDG to solve a linearized transport equation. In order to achieve high order accuracy in time, the SLDG is coupled with the high order RKEI that decomposes the nonlinear transport problem into a sequence of linearized transport equations. This section ends with the algorithm flowcharts of SLDG-RKEI with the adaptive time-stepping algorithm for the nonlinear Vlasov-Poisson and guiding center Vlasov systems.

2.1 The SLDG scheme for linear transport problems

We consider the general nonlinear transport equation in the form of (1.5) for two-dimensional problems in a rectangular domain Ω . In the special case when $\mathbf{P}(u; \mathbf{x}, t) = (P_1(x, y, t), P_2(x, y, t))$ does not depend on u , the model problem (1.5) is linear and can be evolved by the SLDG scheme [2] by accurately tracking characteristics with the velocity field \mathbf{P} .

We partition the domain Ω by a set of non-overlapping tensor-product rectangular elements A_j , $j = 1, \dots, J$, and define the finite dimensional DG approximation space, $\mathbf{V}_h^k = \{v_h : v_h|_{A_j} \in P^k(A_j)\}$, where $P^k(A_j)$ denotes the set of polynomials of degree at most k over $A_j = [x_j^l, x_j^r] \times [y_j^b, y_j^t]$, where element centers and sizes are $x_j = \frac{x_j^l + x_j^r}{2}$, $y_j = \frac{y_j^b + y_j^t}{2}$, $\Delta x_j = x_j^r - x_j^l$, $\Delta y_j = y_j^t - y_j^b$ respectively. In the SLDG framework, we let the test function $\psi(x, y, t)$ satisfy the adjoint problem with $\Psi \in P^k(A_j)$,

$$\begin{cases} \psi_t + P_1(x, y, t)\psi_x + P_2(x, y, t)\psi_y = 0, \\ \psi(t = t_{n+1}) = \Psi. \end{cases} \quad (2.1)$$

Then, we have the identity

$$\frac{d}{dt} \int_{\tilde{A}_j(t)} u(x, y, t) \psi(x, y, t) dx dy = 0, \quad (2.2)$$

where $\tilde{A}_j(t)$ is the dynamic cell, moving from the Eulerian cell A_j at t^{n+1} , i.e., $A_j = \tilde{A}_j(t^{n+1})$, backward in time by following the characteristics trajectories, see eq. (2.4). We denote $\tilde{A}_j(t^n)$ as A_j^* , i.e., the upstream cell bounded by the red curves in Figure 2.1. The SLDG method is defined

as follows. Given $u^n \in \mathbf{V}_h^k$, we seek $u^{n+1} \in \mathbf{V}_h^k$, such that for $\forall \Psi \in P^k(A_j)$, $j = 1, \dots, J$,

$$\int_{A_j} u^{n+1} \Psi dx dy = \int_{A_j^*} u^n \psi(x, y, t^n) dx dy. \quad (2.3)$$

To update u^{n+1} , we need to properly evaluate the right-hand side (RHS) of (2.3), the procedure of which we briefly review below. In particular, we only review P^1 SLDG with quadrilateral approximation; to achieve third order accuracy, one can use the quadratic-curved quadrilateral approximation and P^2 polynomial solution space, see [2] for more details regarding implementation.

1. **Characteristics tracing.** Denote c_q , $q = 1, \dots, 4$ as the four vertices of A_j with the coordinates $(x_{j,q}, y_{j,q})$. We trace characteristics backward in time to t^n for the four vertices by numerically solving the characteristics equations,

$$\begin{cases} \frac{dx(t)}{dt} = P_1(x(t), y(t), t), \\ \frac{dy(t)}{dt} = P_2(x(t), y(t), t), \\ x(t^{n+1}) = x_{j,q}, \\ y(t^{n+1}) = y_{j,q}, \end{cases} \quad (2.4)$$

and obtain c_q^* with the new coordinate $(x_{j,q}^*, y_{j,q}^*)$, $q = 1, \dots, 4$. For example, see c_4 and c_4^* in Figure 2.1. The upstream cell A_j^* can be approximated by a quadrilateral determined by the four vertices c_q^* .

2. **Evaluating the integrals over the upstream cells.** Note that u^n is a piecewise polynomial based on the partition. Then the integral over A_j^* has to be evaluated subregion-by-subregion. To this end, we denote $A_{j,l}^*$ as a non-empty overlapping region between the upstream cell A_j^* and the background grid cell A_l , i.e., $A_{j,l}^* = A_j^* \cap A_l$, $A_{j,l}^* \neq \emptyset$, and define the index set $\varepsilon_j^* := \{l | A_{j,l}^* \neq \emptyset\}$, see Figure 2.1 (b). The detailed procedure of detecting $A_{j,l}^*$ can be found in [2]. The integral over the upstream cell A_j^* is broken up into the following integrals,

$$\int_{A_j} u^{n+1} \Psi dx dy = \sum_{l \in \varepsilon_j^*} \int_{A_{j,l}^*} u^n \psi(x, y, t^n) dx dy. \quad (2.5)$$

Furthermore, $\psi(x, y, t^n)$ is not a polynomial in general, posing additional challenges for evaluating the integrals on the RHS of (2.5). On the other hand, if the velocity field \mathbf{P} is smooth, then $\psi(x, y, t^n)$ is smooth accordingly and can be well approximated by a polynomial. The following procedure is then proposed.

- (a) *Least-squares approximation of test function $\psi(x, y, t^n)$.* We use a least-squares procedure to approximate the test function $\psi(x, y, t^n)$ by a polynomial, based on the fact that ψ stays constant along characteristics. In particular, for $k = 1$, we reconstruct a P^1 polynomial $\Psi^*(x, y)$ by least-squares with the interpolation constraints

$$\Psi^*(x_{j,q}^*, y_{j,q}^*) = \Psi(x_{j,q}, y_{j,q}), \quad q = 1, \dots, 4.$$

Then,

$$\sum_{l \in \varepsilon_j^*} \int_{A_{j,l}^*} u^n \psi(x, y, t^n) dx dy \approx \sum_{l \in \varepsilon_j^*} \int_{A_{j,l}^*} u^n \Psi^*(x, y) dx dy. \quad (2.6)$$

- (b) *Line integral evaluation via Green's theorem.* Note that the integrands on the RHS of (2.6) are piecewise polynomials. To further simplify the implementation, we make use of Green's theorem. We first introduce two auxiliary polynomial functions $P(x, y)$ and $Q(x, y)$ such that

$$-\frac{\partial P}{\partial y} + \frac{\partial Q}{\partial x} = u(x, y, t^n) \Psi^*(x, y).$$

Then area integral $\int_{A_{j,l}^*} u^n \Psi^*(x, y) dx dy$ can be converted into line integrals via Green's theorem, i.e.,

$$\int_{A_{j,l}^*} u(x, y, t^n) \Psi^*(x, y) dx dy = \oint_{\partial A_{j,l}^*} P dx + Q dy, \quad (2.7)$$

see Figure 2.1 (b). Note that the choices of P and Q are not unique, but the value of the line integrals is independent of the choices. These line integrals are organized into line integrals along inner segments and outer segments, for which numerical quadrature rules are applied to evaluate the line integrals, see Figure 2.2.

3. For applications when the u function should stay positive due to its physical meaning (e.g. density, pressure, etc.), a positivity preserving limiter [20] could be added to preserve the positivity of the solution, since the cell average on the upstream cells stay positive.

2.2 SLDG for nonlinear models using Runge-Kutta exponential integrators

For a general nonlinear model in the form of (1.5), per time step evolution from t^n to t^{n+1} , if we freeze the velocity field $\mathbf{P}(u)$ at t^n , the nonlinear problem is linearized around u^n as follows

$$u_t + \nabla \cdot (\mathbf{P}(u^n)u) = 0. \quad (2.8)$$

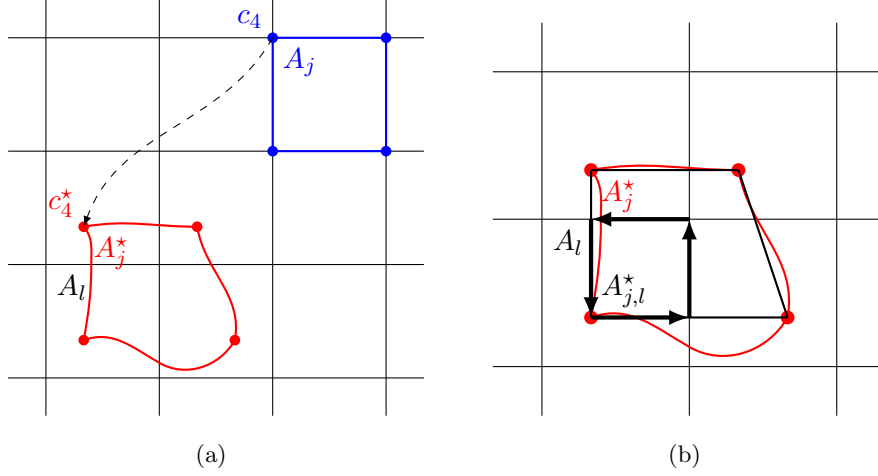


Figure 2.1: Schematic illustration of the SLDG formulation in two dimension: quadrilateral approximation to an upstream cell.

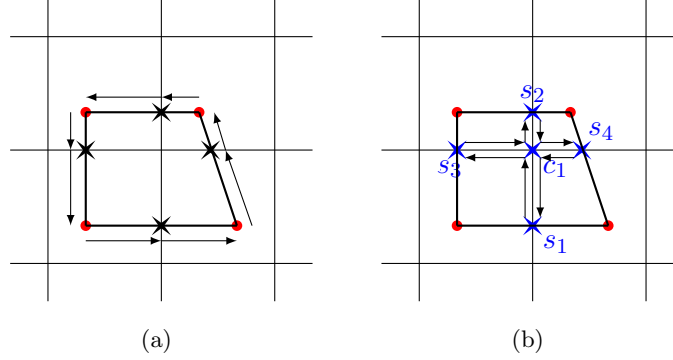


Figure 2.2: Searching algorithm for outer (left) and inner (right) segments.

One can apply a SL scheme (e.g. the SLDG method described above) to the linearized model (2.8), for which we adopt the notation of $SLDG(\mathbf{P}(u^n), \Delta t)$ for the update of solution from u^n to u^{n+1} , i.e.

$$u^{n+1} = SLDG(\mathbf{P}(u^n), \Delta t)(u^n). \quad (2.9)$$

Notice that due to the linearization of the velocity field \mathbf{P} around u^n , there is a first order local truncation error in the temporal direction. To realize a high order temporal discretization, one could develop some strategies to track characteristics of the nonlinear dynamics, see [3] for nonlinear Vlasov-Poisson and [4] for the nonlinear guiding center Vlasov models. However, these strategies are problem-dependent and could be very algebraically involved for implementations. Here in this paper, we propose to adopt the RKEI scheme, which offers a unified framework and a black-box procedure for achieving high order temporal accuracy when coupled with the SLDG method

for solving nonlinear problems. We will first review the RKEI to solve the ordinary differential equations (ODEs) [8]; then it is recognized that the exponential integrator for linear ODEs is equivalent to a semi-Lagrangian update of the solution for linear transport problems, if the spatial dimensions are kept continuous without numerical discretizations. With these observations, one can couple the high order RKEI with SLDG scheme for nonlinear dynamics.

Review of the RKEI for nonlinear ODE systems. Consider a nonlinear ODE model of size N in the form of

$$\frac{dY(t)}{dt} = C(Y)Y, \quad Y(t=0) = Y_0, \quad (2.10)$$

where $C(Y)$ is a matrix-value function of size $N \times N$ that may depend on the solution $Y(t)$. In each time step, if we freeze $C(Y)$ at $C(Y^n)$, then we have a linearized problem $\frac{dY(t)}{dt} = C(Y^n)Y \doteq C^n Y$, for which one can apply an exponential integrator to update the solution from Y^n to Y^{n+1} with a first order local truncation error:

$$Y^{n+1} = \exp(C^n \Delta t) Y^n. \quad (2.11)$$

To improve the accuracy of the above first order scheme, a class of commutator-free exponential integrators can be used. The idea is to achieve high order temporal accuracy via taking composition of a sequence of linear solvers by freezing coefficients, which can be explicitly computed as a linear combination of $C(Y)$ from previous RK stages. In particular, the algorithm flowchart for the RKEI method is summarized as follows.

Algorithm 1: The commutator-free RKEI method [8].

```

 $p = Y^n$ 
for  $r = 1 : s$  do
     $Y_r = \exp(\Delta t \sum_k \alpha_{r,J^{(r)}}^k C(Y_k)) \cdots \exp(\Delta t \sum_k \alpha_{r1}^k C(Y_k)) p$ 
end
 $Y^{n+1} = \exp(\Delta t \sum_k \beta_J^k C(Y_k)) \cdots \exp(\Delta t \sum_k \beta_1^k C(Y_k)) p$ 

```

Here $J^{(r)}$ represents the number of exponentials one has to take per RK stage. The RKEI method can be represented by the Butcher tableau in Table 2.1. It is shown, in [6] by matching

$$\begin{array}{c|c} \mathbf{c} & A \\ \hline & \mathbf{b} \end{array}$$

Table 2.1: A Butcher tableau for RKEI method, where $a_{ik} = \sum_{l=1}^{J^{(i)}} \alpha_{i,l}^k$ and $b_k = \sum_{l=1}^{J^{n+1}} \beta_l^k$, which merges $J^{(i)}$ rows into one row in each stage i .

order conditions, that Butcher tableaus of many first and second order RK methods give the RKEI

methods of the same order; but for third order RKEI method J for some RK stages must be at least 2. In this paper, we will also consider some other Butcher Tableaus from [8, 6] as listed in Appendix A.

Example 2.1. A simple example is a first order exponential integrator, which is represented in Table 2.2.

0	0
1	

Table 2.2: CF1 [14].

It gives a simple first order method for the nonlinear model (1.5),

$$\begin{aligned} Y^{(1)} &= Y^n \\ Y^{n+1} &= \exp(\Delta t C(Y^{(1)})) Y^n. \end{aligned} \tag{2.12}$$

A third order RKEI method in [6] can be represented by the following Butcher tableau,

0			
$\frac{1}{2}$	$\frac{1}{2}$		
$\frac{1}{2}$	-1	2	
1	$\frac{1}{12}$	$\frac{1}{3}$	$-\frac{1}{4}$
	$\frac{1}{12}$	$\frac{1}{3}$	$\frac{5}{12}$

Table 2.3: CF3G

with which, the RKEI scheme for the nonlinear ODE system (2.10) reads

$$\begin{aligned} Y^{(1)} &= Y^n \\ Y^{(2)} &= \exp\left(\frac{1}{2}\Delta t C(Y^{(1)})\right) Y^n \\ Y^{(3)} &= \exp\left(\Delta t(-C(Y^{(1)}) + 2C(Y^{(2)}))\right) Y^n \\ Y^{n+1} &= \exp\left(\Delta t\left(\frac{1}{12}C(Y^{(1)}) + \frac{1}{3}C(Y^{(2)}) + \frac{5}{12}C(Y^{(3)})\right)\right) \\ &\quad \exp\left(\Delta t\left(\frac{1}{12}C(Y^{(1)}) + \frac{1}{3}C(Y^{(2)}) - \frac{1}{4}C(Y^{(3)})\right)\right) Y^n. \end{aligned}$$

SLDG-RKEI for nonlinear transport problems. It was recognized in [6] that the SL update of the solution (2.9) of a linearized transport problem is equivalent to applying the exponential integrator to the linearized ODE system (2.11), as both of the methods evolve the differential

equation *exactly* for a time step. Thus, the high order RKEI method developed in [8] can be systematically coupled with the SLDG scheme described above for solving nonlinear dynamics (1.5) in a black-box manner. In particular, a first order RKEI scheme with Butcher tableau (2.2) gives rise to a first order scheme (2.9); and a third order RKEI scheme with Butcher tableau (2.3) coupling with the SLDG scheme reads as

$$\begin{aligned}
u^{(1)} &= u^n \\
u^{(2)} &= SLDG\left(\frac{1}{2}\mathbf{P}(u^{(1)}), \Delta t\right) u^n \\
u^{(3)} &= SLDG\left(-\mathbf{P}(u^{(1)}) + 2\mathbf{P}(u^{(2)}), \Delta t\right) u^n \\
u^{n+1} &= SLDG\left(\frac{1}{12}\mathbf{P}(u^{(1)}) + \frac{1}{3}\mathbf{P}(u^{(2)}) + \frac{5}{12}\mathbf{P}(u^{(3)}), \Delta t\right) \\
&\quad SLDG\left(\frac{1}{12}\mathbf{P}(u^{(1)}) + \frac{1}{3}\mathbf{P}(u^{(2)}) - \frac{1}{4}\mathbf{P}(u^{(3)}), \Delta t\right) u^n.
\end{aligned} \tag{2.13}$$

The scheme is named as “SLDG-CF3G” for short. The scheme is of high order accuracy in both space and time.

2.3 Algorithm flowchart for nonlinear transport problems

Below we summarize the flowchart of the SLDG-RKEI method for the nonlinear transport problems, such as the nonlinear Vlasov-Poisson and the guiding center Vlasov systems. We borrow notations for RKEI schemes from Algorithm 1.

Algorithm 2: SLDG-RKEI algorithm to update solution from t^n to t^{n+1} for nonlinear transport problems in the form of (1.5).

```

for  $r = 1 : s$ 
  • Let  $u^{[1]} = u^n$ , and  $\mathbf{P}(u^{(r)})$  be the velocity field  $\mathbf{P}(u)$  frozen at the stage  $r$ .
  for  $l = 1 : J^{(r)}$ 
    •  $u^{[l+1]} = SLDG(\sum_k \alpha_{rl}^k \mathbf{P}(u^{(k)}), \Delta t) u^{[l]}$ .
  end
  • Let  $u^{(r)} = u^{[J^{(r)}+1]}$ .
end
• Let  $u^{[1]} = u^n$ .
for  $l = 1 : J$ 
  •  $u^{[l+1]} = SLDG(\sum_k \beta_l^k \mathbf{P}(u^{(k)}), \Delta t) u^{[l]}$ .
end
•  $u^{n+1} = u^{[J+1]}$ .

```

We make the following two remarks on the flow chart for the Vlasov-Poisson system (1.1) and the guiding center Vlasov model (1.3) applications.

1. To freeze the velocity field, one can apply an LDG method in [1, 9, 5, 16] for (1.2) and (1.4), respectively. The resulting velocity fields are discontinuous. In this paper, we take the average of the velocity field in tracking characteristics. A post-processing technique [17] could be added for smooth the discontinuous velocity field, for which we plan to explore in the future.

2. In [4], an adaptive time-stepping algorithm is introduced for the systems (1.1) and (1.3), based on controlling the L^∞ norm of relative deviation of upstream cells' area. This adaptive time-stepping algorithm is summarized as Algorithm 3 below and can be applied to each RK stage of the SLDG-RKEI algorithm in order to adaptively choose time stepping sizes.

Algorithm 3: Adaptive Time-Stepping Algorithm in an SLDG-RKEI method.

Let A_j be an Eulerian cell and A_j^* be its upstream cell in a stage of the SLDG-RKEI scheme.

Compute $\theta = \max_j \left| \frac{\text{area}(A_j^*) - \text{area}(A_j)}{\text{area}(A_j)} \right|$.

Let δ_M and δ_m be prescribed thresholds for decreasing and increasing CFL number. In our simulations, $\delta_M = 1\%$ and $\delta_m = 0.05\%$.

if $\theta > \delta_M$, **then** $irefine = 1$ we decrease CFL (e.g. $CFL = \max(CFL - 1, CFL_{\min})$), and restart the SLDG-RKEI scheme with the updated CFL .

else if $\theta < \delta_m$, **then** $irefine = 0$, we increase CFL (e.g. $CFL = \min(CFL + 1, CFL_{\max})$) and restart the SLDG-RKEI scheme with the updated CFL .

else Continue.

end if

3 Numerical results

3.1 Nonlinear Vlasov dynamics

In this section, we present numerical results of the SLDG-RKEI for the nonlinear Vlasov-Poisson system and the Guiding center Vlasov model. Unless otherwise noted, we use the following notations: the SLDG method with P^k polynomial basis is denoted as P^k SLDG; we use the notation without or with -QC to denote quadrilateral or quadratic-curved (QC) quadrilateral approximation to upstream cells. We set the time step as

$$\Delta t = \frac{CFL}{\frac{a}{\Delta x} + \frac{b}{\Delta y}}, \quad (3.1)$$

where a and b are maximum transport speeds in x - and y - directions, respectively.

Example 3.1. (*VP system: strong Landau damping.*) Consider strong Landau damping for the VP system with the initial condition being a perturbed equilibrium

$$f(x, v, t = 0) = \frac{1}{\sqrt{2\pi}}(1 + \alpha \cos(kx)) \exp\left(-\frac{v^2}{2}\right), \quad (3.2)$$

where $\alpha = 0.5$ and $k = 0.5$. The computational domain is $[0, 4\pi] \times [-2\pi, 2\pi]$. This problem has been numerically investigated by several authors, e.g. see [19, 21, 12].

In Table 3.4, we first test the spatial convergence of the SLDG methods with the third order temporal scheme, CF3C03, whose Butcher tableau is presented in the Appendix. The well-known time reversibility of the VP system [11] is used to test the order of convergence. In particular, one can integrate the VP system forward to some time T , and then reverse the velocity field of the solution and continue to integrate the system by the same amount of time T . Then, the solution should recover the initial condition with reverse velocity field, which can be used as a reference solution. We show the L^1 , L^2 , and L^∞ errors and the corresponding orders of convergence for P^k SLDG(-QC)+CF3C03 scheme, $k = 1, 2$ with $CFL = 0.1$ in Table 3.4. We observe the second order convergence for P^1 SLDG scheme; we observe a second order convergence for P^2 SLDG scheme with quadrilateral approximation to upstream cells, and a third order convergence for the P^2 SLDG-QC scheme.

We then test the temporal convergence of different temporal schemes by the strong Landau damping test case integrated to $T = 5$. In order to minimize the errors from the spatial discretization, we adopt the P^2 SLDG-QC scheme with a fixed mesh of 200×200 cells. The reference solution is computed by the P^2 SLDG-QC scheme with the same mesh but using a small $CFL = 0.1$. We report plots of L^1 and L^∞ errors versus the CFL number of different RKEI methods in Figure 3.3. The Butcher tableau of these RKEI methods can be found in the previous Section as well as in the Appendix. We make the following observations: (1) expected temporal orders of convergence are observed for various SLDG-RKEI method; (2) CFL s can be taken to be as large as 50, which is much larger than that for an Eulerian RKDG method, whose CFL upper bound is $1/(2k+1)$ with k being the degree of the polynomial; (3) For the purpose of comparison, we plot results from the SLDG method coupled with a predictor-corrector way of tracking characteristics [3]. It is observed that third order temporal accuracy is numerically achieved for all third order time integrators; the error magnitudes from SLDG-RKEI schemes are observed to be smaller.

There are several conserved quantities in the VP system which should remain constant in time.

Table 3.4: Strong Landau damping. $T = 0.5$. Use the time reversibility of the VP system. Order of accuracy in space for P^k SLDG(-QC)+CF3C03 scheme, $k = 1, 2$. We set $CFL = 0.1$ so that the spatial error is the dominant error.

Mesh	L^1 error	Order	L^2 error	Order	L^∞ error	Order
P^1 SLDG+CF3C03						
32^2	5.88E-04		1.21E-03		1.18E-02	
64^2	1.50E-04	1.97	3.17E-04	1.94	3.49E-03	1.76
96^2	6.67E-05	1.99	1.42E-04	1.97	1.61E-03	1.91
128^2	3.76E-05	2.00	8.06E-05	1.98	9.19E-04	1.95
160^2	2.41E-05	2.00	5.17E-05	1.99	5.93E-04	1.97
P^2 SLDG+CF3C03						
32^2	9.59E-05		2.18E-04		1.95E-03	
64^2	2.43E-05	1.98	5.57E-05	1.97	5.05E-04	1.95
96^2	1.09E-05	1.98	2.50E-05	1.98	2.26E-04	1.99
128^2	6.15E-06	1.99	1.41E-05	1.98	1.27E-04	1.99
160^2	3.94E-06	1.99	9.07E-06	1.99	8.15E-05	2.00
P^2 SLDG-QC+CF3C03						
32^2	3.69E-05		8.39E-05		1.09E-03	
64^2	4.39E-06	3.07	1.03E-05	3.03	1.38E-04	2.98
96^2	1.28E-06	3.04	3.02E-06	3.02	4.09E-05	3.00
128^2	5.37E-07	3.02	1.27E-06	3.01	1.71E-05	3.03
160^2	2.74E-07	3.02	6.50E-07	3.01	9.97E-06	2.42

These include the L^p norm, kinetic energy and entropy:

- L^p norm, $1 \leq p \leq \infty$:

$$\|f\|_p = \left(\int_v \int_x |f(x, v, t)|^p dx dv \right)^{\frac{1}{p}}, \quad (3.3)$$

- Energy:

$$\text{Energy} = \int_v \int_x f(x, v, t) v^2 dx dv + \int_x E^2(x, t) dx, \quad (3.4)$$

- Entropy:

$$\text{Entropy} = \int_v \int_x f(x, v, t) \log(f(x, v, t)) dx dv. \quad (3.5)$$

In Figure 3.4, we plot the time evolution of the relative deviation of L^1 and L^2 norms of the solution as well as the discrete kinetic energy and entropy. Here we choose to present only a few representative RKEI schemes and run our simulations with $CFL = 10$. A few observations can be made: (1) due to the truncation of the velocity domain, the error for the relative deviation of L^1 norm is on the of 10^{-9} ; (2) the SLDG with higher degree polynomial does a better job in conserving these physical norms than the SLDG with lower degree polynomial; (3) there is little difference in

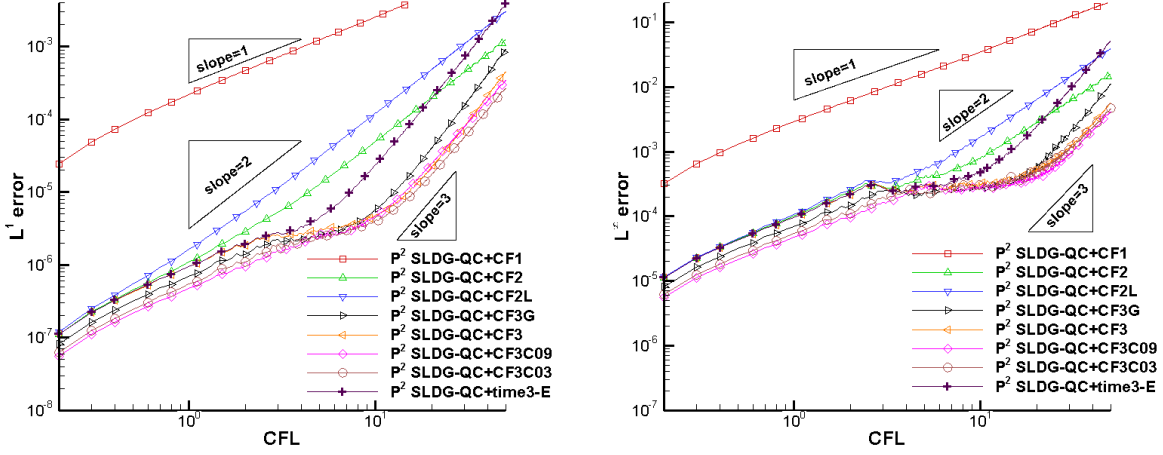


Figure 3.3: Plots of error versus the CFL number for solving strong Landau damping at $T = 5$. Temporal order of convergence in L^1 and L^∞ norm of P^2 SLDG-QC scheme with various temporal schemes by comparing numerical solutions with a reference solution from the corresponding scheme with $CFL = 0.1$. The mesh of 160×160 is used. P^2 SLDG-QC+time3-E is P^2 SLDG-QC with the third order prediction correction method in [3].

the performance of preserving norms for the P^k SLDG with various same order temporal scheme including the prediction-correction method. In Figure 3.5, we present the surface plots of the solutions at $T = 40$ computed by P^k SLDG ($k = 1, 2$) with the mesh of 160×160 elements. The numerical solution of P^2 SLDG outperform that of P^1 SLDG in terms of resolution.

Example 3.2. (The guiding center Vlasov system: spatial accuracy and convergence test). Consider the guiding center Vlasov model on the domain $[0, 2\pi] \times [0, 2\pi]$ with the initial condition

$$\omega(x, y, 0) = -2 \sin(x) \sin(y) \quad (3.6)$$

and the periodic boundary condition. The exact solution stays stationary. We test the spatial convergence of the proposed SLDG methods with the third order temporal scheme, CF3C03, for solving the guiding center Vlasov model up to time $T = 1$ and report these results in Table 3.5. We observe the expected second order of convergence for P^1 SLDG+ P^2 LDG in L^1 , L^2 , and L^∞ norms. For P^2 SLDG scheme with quadrilateral approximation to upstream cells, the error magnitude will be reduced but still second order. For P^2 SLDG scheme with quadratic-curved quadrilateral approximation to upstream cells, we observe the third order of convergence in L^1 and L^2 norm but the second order of convergence in L^∞ norm.

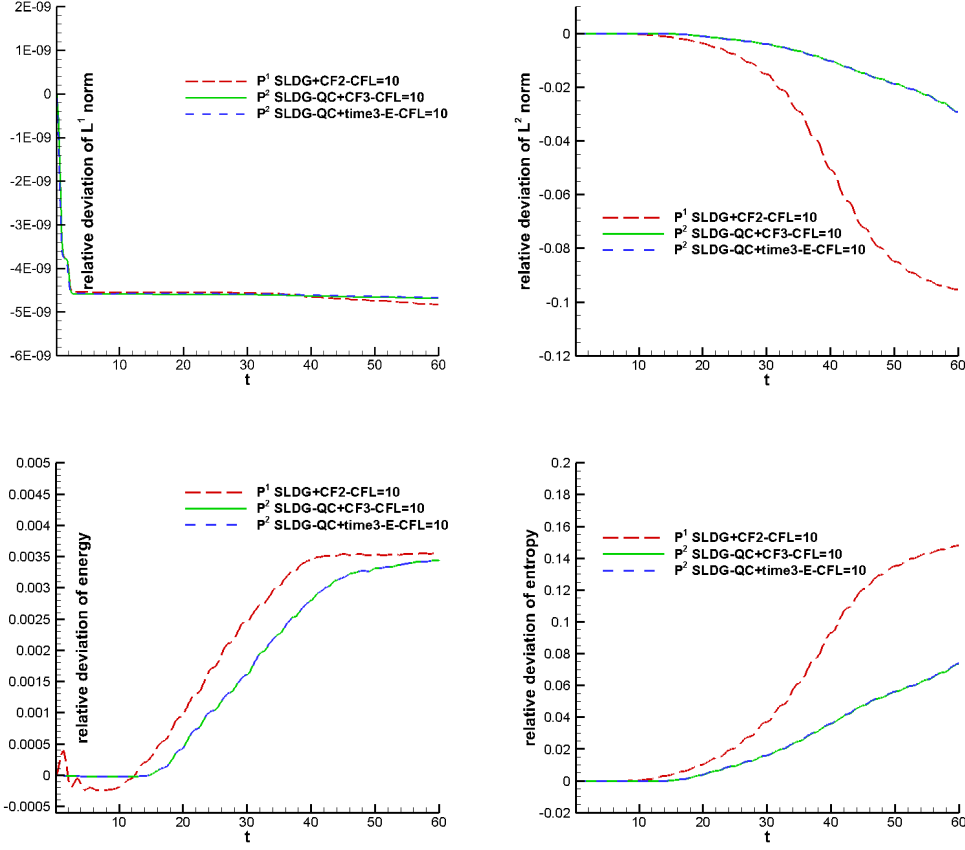


Figure 3.4: Strong Landau damping. Time evolution of the relative deviation of L^1 (upper left) and L^2 (upper right) norms of the solution as well as the discrete kinetic energy (lower left) and entropy (lower right). We use a mesh of 160×160 cells and $CFL = 10$. P^2 SLDG-QC+time3-E is P^2 SLDG-QC with the third order prediction correction method in [3].

Example 3.3. (The guiding center Vlasov model: Kelvin-Helmholtz instability problem). This is the two-dimensional guiding center model problem (1.3) with the initial condition

$$\rho_0(x, y) = \sin(y) + 0.015 \cos(kx) \quad (3.7)$$

and periodic boundary conditions on the domain $[0, 4\pi] \times [0, 2\pi]$. We let $k = 0.5$, which will create a Kelvin-Helmholtz instability [18], which is well studied numerically by many authors before (e.g. see [22, 4]).

First, we test the temporal convergence of the proposed SLDG method with different temporal schemes by computing this problem up to $T = 5$. In order to minimize the errors from the spatial scheme, we adopt the P^2 SLDG-QC scheme with P^3 LDG method using a fixed mesh of 120×120 cells. The reference solution is computed by the same scheme with the same mesh but using a small

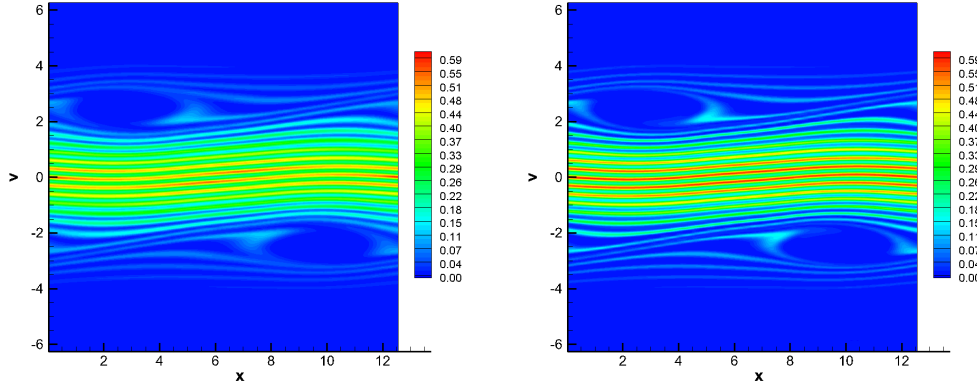


Figure 3.5: Surface plots of the numerical solutions for the strong Landau damping at $T = 40$. We use a mesh of 160×160 cells and $CFL = 10$. left: P^1 SLDG+CF2; right: P^2 SLDG-QC+CF3C03.

Table 3.5: The guiding center Vlasov system on the domain $[0, 2\pi] \times [0, 2\pi]$ with the initial condition $\omega(x, y, 0) = -2 \sin(x) \sin(y)$. Periodic boundary conditions in two directions. $T = 1$. $CFL = 1$.

Mesh	L^1 error	Order	L^2 error	Order	L^∞ error	Order
P^1 SLDG+ P^2 LDG+CF3C03						
20^2	1.39E-02		1.88E-02		1.06E-01	
40^2	3.66E-03	1.93	4.97E-03	1.92	3.12E-02	1.76
60^2	1.65E-03	1.97	2.24E-03	1.97	1.44E-02	1.90
80^2	9.37E-04	1.96	1.27E-03	1.95	8.27E-03	1.93
100^2	6.01E-04	1.99	8.17E-04	1.99	5.34E-03	1.96
P^2 SLDG+ P^3 LDG+CF3C03						
20^2	4.52E-03		6.61E-03		5.60E-02	
40^2	1.02E-03	2.14	1.53E-03	2.11	1.49E-02	1.91
60^2	4.30E-04	2.14	6.37E-04	2.17	6.76E-03	1.95
80^2	2.54E-04	1.82	3.80E-04	1.79	3.89E-03	1.92
100^2	1.52E-04	2.30	2.29E-04	2.27	2.52E-03	1.94
P^2 SLDG-QC+ P^3 LDG+CF3C03						
20^2	2.13E-03		2.77E-03		2.06E-02	
40^2	2.73E-04	2.97	3.63E-04	2.93	4.72E-03	2.13
60^2	8.11E-05	2.99	1.09E-04	2.96	2.06E-03	2.04
80^2	3.48E-05	2.94	4.74E-05	2.91	1.14E-03	2.05
100^2	1.77E-05	3.02	2.44E-05	2.98	7.28E-04	2.02

$CFL = 0.1$. We report plots of L^1 and L^∞ errors versus the CFL number in Figure 3.6. Some observations can be concluded from Figure 3.6: (1) expected order of convergence is observed for all temporal schemes; and CFL number can be taken to be as large as 50; (2) by comparing the error magnitudes, CF2L performs better than CF2 and CF3C09 performs the best.

For this problem, the energy $\|\mathbf{E}\|_{L^2}^2 = \int_{\Omega} \mathbf{E} \cdot \mathbf{E} dx dy$ and enstrophy $\|\rho\|_{L^2}^2 = \int_{\Omega} \rho^2 dx dy$ should

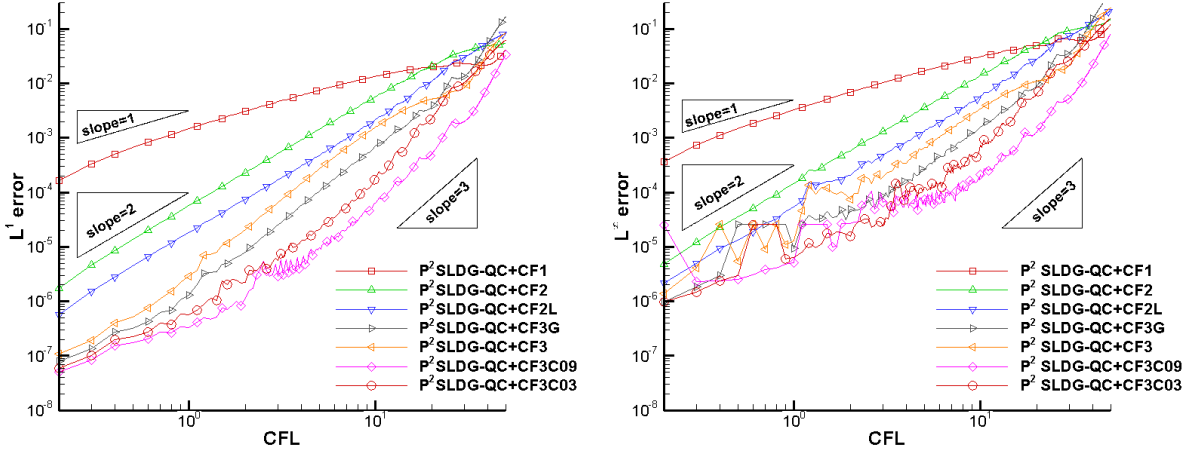


Figure 3.6: Plots of error versus the CFL number for solving the Kelvin-Helmholtz instability at $T = 5$. Temporal order of convergence in L^1 and L^∞ norm of P^2 SLDG-QC+ P^3 LDG with various temporal schemes by comparing numerical solutions with a reference solution from the corresponding scheme with $CFL = 0.1$. The mesh of 120×120 is used.

remain constant in time. Tracking relative deviations of these quantities provides a good measurement of the quality of numerical schemes. We evaluate the performance of proposed schemes with a large $CFL = 5$ for the Kelvin-Helmholtz instability for a long-time simulation. Figure 3.7 shows surface plots of the numerical solutions for the Kelvin-Helmholtz instability at $T = 40$, and Figure 3.8 reports the time evolution of the relative deviation of energy and enstrophy of the numerical solutions. From Figure 3.7, we can observe that P^2 SLDG-QC outperforms P^1 SLDG, with the same mesh. From Figure 3.8, we can observe that higher order schemes performs better than lower order ones in terms of enstrophy; and different RKEI schemes have comparable performances.

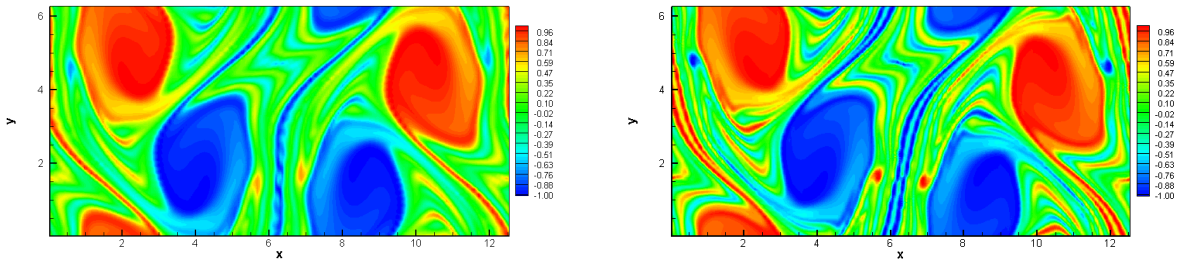


Figure 3.7: Surface plots of the numerical solutions for the Kelvin-Helmholtz instability at $T = 40$. We use a mesh of 100×100 cells and $CFL = 5$. Left: P^1 SLDG+ P^2 LDG+CF2. Right: P^2 SLDG-QC+ P^3 LDG+CF3C03.

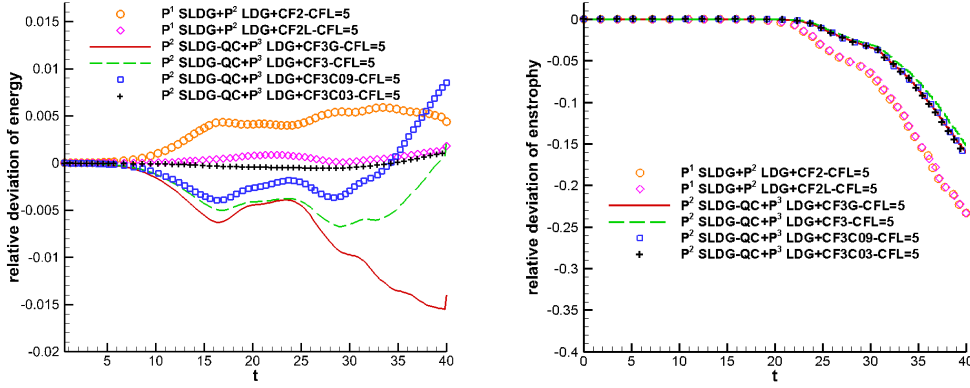


Figure 3.8: Time evolutions of the relative deviation of energy (left) and enstrophy (right) for the proposed SLDG schemes for the Kelvin-Helmholtz instability problem. The mesh of 100×100 cells is used.

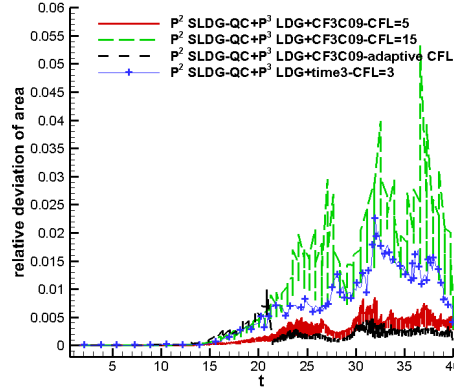


Figure 3.9: Kelvin-Helmholtz instability. Use a mesh of 100×100 cells. Performances of P^2 SLDG-QC with different CFL s as well as the adaptive time-stepping algorithm in L^∞ norm of the relative deviation of areas of upstream cells.

Next, we test the performance of proposed schemes with the larger time-stepping size for the Kelvin-Helmholtz instability. Note that the SLDG schemes with the very large time-stepping size might be subject to extreme distortion of upstream cells. Due the divergence-free constraint on the electric field of the guiding center Vlasov model, the areas of upstream cells should be preserved for the exact solution. If at the discrete level, the areas of upstream cells are preserved, the local maximum principle in terms of cell averages will be maintained; if the area of a numerical upstream cell greatly deviates from the actual area, unphysical numerical oscillations may appear. In particular, in Figure 3.9, by comparing the relative deviation of area of P^2 SLDG-QC+ P^3

LDG+time3 with $CFL = 3$ and P^2 SLDG-QC+ P^3 LDG+CF3C09 with the larger $CFL = 5$, we observe that the latter one outperforms the former one. It shows that the SLDG schemes with the third order exponential integrators can allow for a larger CFL . Then we test the performance of proposed schemes with a huge $CFL = 15$. We present surface plots of the numerical solutions of the schemes under $CFL = 15$ at $T = 40$ in Figure 3.10. From Figure 3.10, we can find that P^2 SLDG-QC+ P^3 LDG+CF3C09 performs best, while P^2 SLDG-QC+ P^3 LDG+CF3 performs worst in correctly resolving solution structure. These observations show a good agreement with the accuracy comparison of these schemes presented in Figure 3.6.

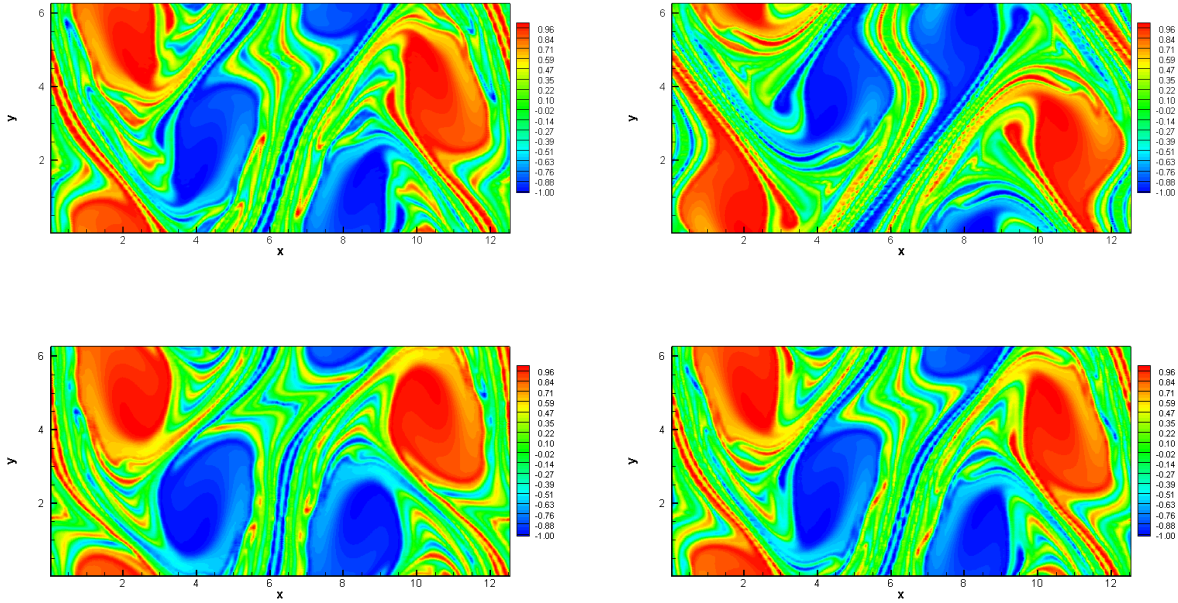


Figure 3.10: Surface plots of numerical solutions for the Kelvin-Helmholtz instability at $T = 40$. We use a mesh of 100×100 cells and huge $CFL = 15$. Top left: P^2 SLDG-QC+ P^3 LDG+CF3G. Top right: P^2 SLDG-QC+ P^3 LDG+CF3. Bottom left: P^2 SLDG-QC+ P^3 LDG+CF3C09. Bottom right: P^2 SLDG-QC+ P^3 LDG+CF3C03.

Numerical verification of the adaptive time-stepping algorithm for the nonlinear transport problems with the divergence-free constraint.

It is observed that different RKEI schemes with $CFL = 5$ have comparable performances, therefore we only present results from one second order and one third order RKEI schemes in Figure 3.7; yet schemes with larger $CFL = 15$ are observed to perform differently as shown in Figure 3.10. In Figure 3.9, we plot the schemes' performance in conserving the L^∞ of the the upstream area under various settings (different schemes,

CFLs, etc.). It is observed that, compared to the scheme with $CFL = 5$, the area of upstream cells from the scheme with $CFL = 15$ has larger deviation. We adopt the relative deviation of areas of upstream cells as an indicator for the adaptive time-stepping algorithm in Section ?? . Figure 3.11 (a) presents the 3D plot of the P^2 SLDG-QC+ P^3 LDG+CF3C09 scheme with adaptive time-stepping algorithm for the Kelvin-Helmholtz instability at $T = 40$, using a mesh of 100×100 cells. Similar resolution is observed when compared with the scheme with $CFL = 5$. Figure 3.11 (b) presents the CFL versus time, which showcases the effectiveness of the adaptive time stepping strategy when the solution gets more complex. Figure 3.12 shows the time evolutions of the relative deviation of energy and enstrophy the scheme with different settings. The adaptive time-stepping scheme can conserve energy much better than the scheme with a fixed large CFL number.

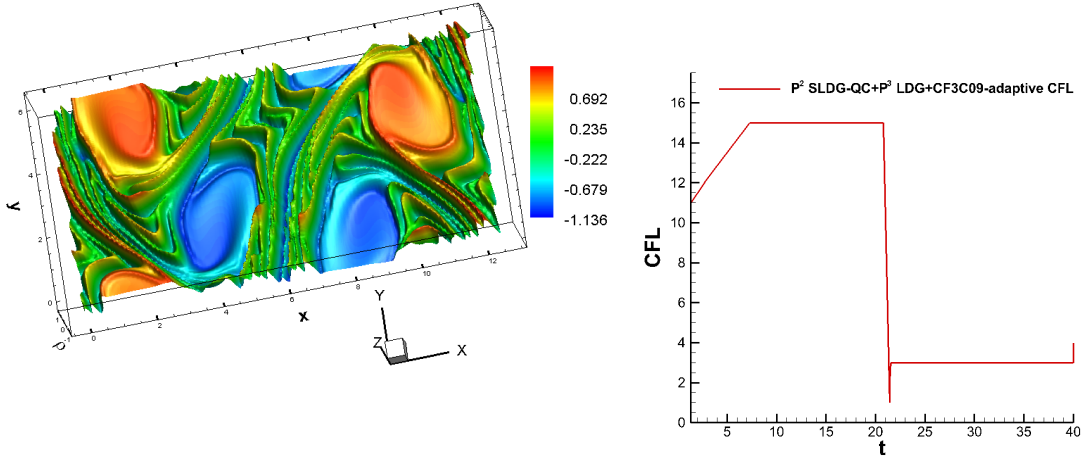


Figure 3.11: The numerical solution of P^2 SLDG-QC+ P^3 LDG+CF3C09 with the adaptive time-stepping algorithm for the Kelvin-Helmholtz instability at $T = 40$, using a mesh of 100×100 cells. Top left: the surface plot of the solution. Top right: the time evolution of CFL versus time. Bottom: the three-dimensional plot of the solution.

3.2 Preliminary numerical tests on Burgers' equation

The focus of the current paper is on the nonlinear Vlasov dynamics, yet the SLDG-RKEI scheme can be applied to general nonlinear hyperbolic conservation laws. In this subsection, we present our preliminary results on applying the SLDG-RKEI schemes to a simple Burgers' equation with shock developments. Notice that for the nonlinear Vlasov dynamics, despite the development of

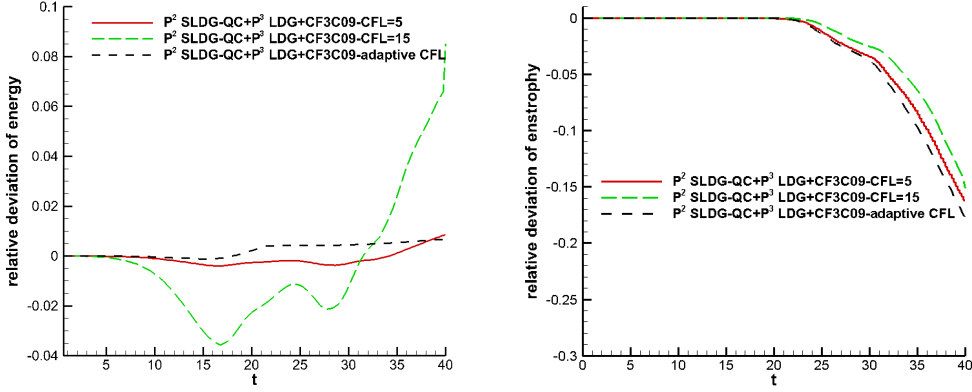


Figure 3.12: The time evolutions of the relative deviation of energy (left) and enstrophy (right) for P^2 SLDG-QC+ P^3 LDG+CF3C09 with the adaptive time-stepping algorithm for the Kelvin-Helmholtz instability problem, compared to that of the same scheme using a $CFL = 5$ as well as that of the same scheme using a larger $CFL = 15$.

filamentation structure as time evolves, shocks form from smooth initial data. We will show below that the development of shocks limit the time stepping size allowed for stability. We consider the 1D Burgers' equation,

$$u_t + \left(\frac{1}{2}u^2\right)_x = 0, \quad (3.8)$$

and rewrite it in the form of

$$u_t + (P(u)u)_x = 0. \quad (3.9)$$

with $P(u) = 1/2u$. We first consider the initial condition $u(x, 0) = 0.5 + \sin(\pi x)$. When $t = 0.5/\pi$, the solution is still smooth. We present the errors and their corresponding orders of convergence in terms of L^1 , L^2 and L^∞ norms in Table 3.6. Expected orders of convergence are observed. Notice that the presented CFL for each scheme is the largest CFL allowed for numerical stability, chopped off to one decimal place; and $\Delta t = \frac{CFL \Delta x}{\max_u f'(u)}$. The maximum CFL allowed for the Burgers' equation seems to be more limited than that for the nonlinear Vlasov dynamics; yet is still larger than those in a RKDG setting which is $1/(2k + 1)$ with k being the polynomial degrees. The left panel of Figure 3.13 presents the solutions of the SLDG-RKEI schemes at $t = 1.5/\pi$ after a shock develops using a mesh of $N = 80$ with $CFL = 0.5$. We also consider a discontinuous initial condition,

$$u(x, 0) = \begin{cases} 1 & \text{if } -1 \leq x < 0, \\ 3 & \text{if } 0 \leq x < 1, \end{cases} \quad (3.10)$$

with periodic boundary condition. The solution of this problem includes one shock and one rarefaction wave. The right panel of Figure 3.13 presents the numerical solutions that well capture the exact solution. Note that the CFL numbers taken here are ad hoc from numerical tests, and the stability property of the scheme for nonlinear problems is still subject to further investigation.

Table 3.6: Burgers's equation $u_t + (u^2/2)_x = 0$ with the initial condition $u(x, 0) = 0.5 + \sin(\pi x)$, $t = 0.5/\pi$.

Mesh	L^1 error	Order	L^2 error	Order	L^∞ error	Order
P^0 SLDG+CF1 with $CFL = 1.2$						
40	2.75E-02		3.85E-02		1.72E-01	
80	1.38E-02	0.99	1.96E-02	0.97	9.09E-02	0.92
160	6.96E-03	0.99	9.95E-03	0.98	4.71E-02	0.95
320	3.49E-03	1.00	5.02E-03	0.99	2.40E-02	0.97
P^1 SLDG+CF2 with $CFL = 1.2$						
40	1.81E-03		2.89E-03		1.66E-02	
80	4.73E-04	1.93	7.57E-04	1.93	4.15E-03	2.00
160	1.20E-04	1.98	1.94E-04	1.97	1.02E-03	2.03
320	3.00E-05	2.00	4.90E-05	1.98	2.50E-04	2.03
P^1 SLDG+CF2L with $CFL = 1.2$						
40	1.79E-03		2.79E-03		1.15E-02	
80	4.69E-04	1.94	7.37E-04	1.92	2.87E-03	2.00
160	1.19E-04	1.97	1.89E-04	1.96	7.00E-04	2.03
320	2.99E-05	1.99	4.78E-05	1.98	1.82E-04	1.95
P^2 SLDG+CF3G with $CFL = 0.7$						
40	1.11E-04		2.50E-04		2.14E-03	
80	1.70E-05	2.71	4.55E-05	2.46	4.94E-04	2.12
160	2.59E-06	2.71	8.31E-06	2.45	1.27E-04	1.95
320	3.79E-07	2.77	1.50E-06	2.47	3.10E-05	2.04
P^2 SLDG+CF3 with $CFL = 0.4$						
40	1.11E-04		2.42E-04		2.10E-03	
80	1.68E-05	2.72	4.47E-05	2.44	4.89E-04	2.10
160	2.54E-06	2.73	8.20E-06	2.45	1.27E-04	1.95
320	3.76E-07	2.75	1.49E-06	2.46	3.09E-05	2.04
P^2 SLDG+CF3C09 with $CFL = 0.7$						
40	1.07E-04		2.40E-04		2.08E-03	
80	1.65E-05	2.69	4.44E-05	2.43	4.88E-04	2.10
160	2.52E-06	2.72	8.18E-06	2.44	1.27E-04	1.95
320	3.73E-07	2.75	1.49E-06	2.46	3.09E-05	2.03
P^2 SLDG+CF3C03 with $CFL = 0.7$						
40	1.08E-04		2.41E-04		2.10E-03	
80	1.65E-05	2.70	4.45E-05	2.44	4.89E-04	2.10
160	2.51E-06	2.72	8.20E-06	2.44	1.27E-04	1.95
320	3.72E-07	2.76	1.49E-06	2.46	3.09E-05	2.04

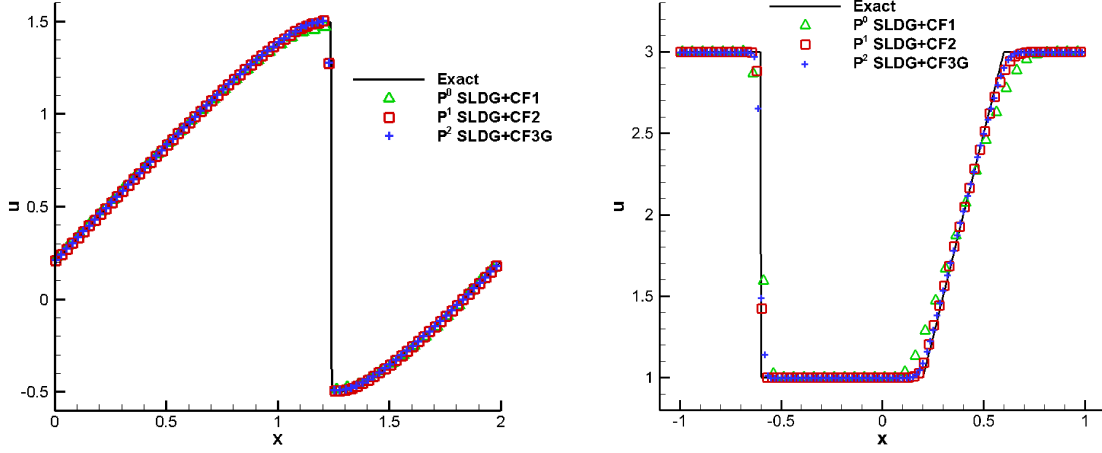


Figure 3.13: Burgers's equation $u_t + (u^2/2)_x = 0$. Left: initial condition $u(x, 0) = 0.5 + \sin(\pi x)$ at $t = 1.5/\pi$. Right: a discontinuous initial condition (3.10) and periodic boundary condition at $t = 0.2$. The meshes of 80 cells and $CFL = 0.5$ are used.

4 Conclusion

In this paper, we propose a high order SLDG-RKEI method for nonlinear Vlasov dynamics. Compared with previous work on semi Lagrangian methods, the new method could be systematically built up to be high order accurate in both spatial and temporal directions, mass conservative, computationally efficient in allowing extra large time stepping sizes and highly effective in resolving nonlinear Vlasov dynamics. Applications of the method to nonlinear Navier-Stokes system will be investigated in our future work. We also test the scheme on the nonlinear Burgers' equation and found CFL constraints similar to those from an Eulerian approach. Further study needs to be performed to better understand the stability of the method.

A Some commutator-free methods

In this appendix we present some different Butcher tableaus of commutator-free methods from [8, 6], which are tested in this paper.

0			
$\frac{1}{2}$		$\frac{1}{2}$	0
—		0	1

Table A.7: CF2

0			
γ	γ		
1	δ	$1 - \delta$	
	0	$1 - \gamma$	γ

Table A.8: CF2L. Here $\gamma = \frac{2-\sqrt{2}}{2}$ and $\delta = \frac{-2\sqrt{2}}{3}$.

0			
γ	γ		
$1 - \gamma$	$\gamma - 1$	$2(1 - \gamma)$	
	0	$\frac{1}{2} - \phi$	$\frac{1}{2} + \phi$
	0	ϕ	$-\phi$

Table A.9: CF3. Here $\gamma = \frac{3+\sqrt{3}}{6}$ and $\phi = \frac{1}{6(2\gamma-1)}$.

0			
γ	γ		
$1 - \gamma$	$\gamma - 1$	$2(1 - \gamma)$	
	α	β	σ
	$-\alpha$	$\frac{1}{2} - \beta$	$\frac{1}{2} - \sigma$

Table A.10: CF3C09. Here $\sigma = (\alpha + \beta(1 - 2\gamma) - \frac{1}{3})/(1 - 2\gamma)$, $\alpha = \frac{1}{2}, \frac{1}{6}$ and $\gamma = \frac{3+\sqrt{3}}{6}$.

0			
$\frac{1}{3}$	$\frac{1}{3}$		
$\frac{2}{3}$	0	$\frac{2}{3}$	
$\frac{3}{3}$	$\frac{1}{3}$	0	0
	$-\frac{1}{12}$	0	$\frac{3}{4}$

Table A.11: CF3C03. [8]

References

- [1] D. Arnold, F. Brezzi, B. Cockburn, and L. Marini. Unified analysis of discontinuous Galerkin methods for elliptic problems. *SIAM Journal on Numerical Analysis*, 39(5):1749–1779, 2002.
- [2] X. Cai, W. Guo, and J.-M. Qiu. A high order conservative semi-Lagrangian discontinuous Galerkin method for two-dimensional transport simulations. *Journal of Scientific Computing*, 73(2-3):514–542, 2017.
- [3] X. Cai, W. Guo, and J.-M. Qiu. A high order semi-Lagrangian discontinuous Galerkin method for Vlasov-Poisson simulations without operator splitting. *Journal of Computational Physics*, 354:529–551, 2018.
- [4] X. Cai, W. Guo, and J.-M. Qiu. A high order semi-Lagrangian discontinuous Galerkin method for the two-dimensional incompressible Euler equations and the guiding center Vlasov model without operator splitting. *Journal of Scientific Computing*, 79(2):1111–1134, 2019.
- [5] P. Castillo, B. Cockburn, I. Perugia, and D. Schötzau. An a priori error analysis of the local discontinuous Galerkin method for elliptic problems. *SIAM Journal on Numerical Analysis*, 38(5):1676–1706, 2000.
- [6] E. Celledoni and B. K. Kometa. Semi-Lagrangian Runge-Kutta exponential integrators for convection dominated problems. *Journal of Scientific Computing*, 41(1):139–164, 2009.
- [7] E. Celledoni, B. K. Kometa, and O. Verdier. High order semi-Lagrangian methods for the incompressible Navier–Stokes equations. *Journal of Scientific Computing*, 66(1):91–115, 2016.
- [8] E. Celledoni, A. Marthinsen, and B. Owren. Commutator-free Lie group methods. *Future Generation Computer Systems*, 19(3):341–352, 2003.
- [9] B. Cockburn and C.-W. Shu. The local discontinuous Galerkin method for time-dependent convection-diffusion systems. *SIAM Journal on Numerical Analysis*, 35(6):2440–2463, 1998.
- [10] N. Crouseilles, M. Mehrenberger, and E. Sonnendrücker. Conservative semi-Lagrangian schemes for Vlasov equations. *Journal of Computational Physics*, 229(6):1927–1953, 2010.

- [11] P. Degond, L. Pareschi, and G. Russo. *Modeling and computational methods for kinetic equations*. Springer Science & Business Media, 2004.
- [12] C.-S. Huang, T. Arbogast, and C.-H. Hung. A semi-Lagrangian finite difference WENO scheme for scalar nonlinear conservation laws. *Journal of Computational Physics*, 322:559–585, 2016.
- [13] B. K. Kometa. On Semi-Lagrangian Exponential Integrators and Discontinuous Galerkin Methods. In *AIP Conference Proceedings*, volume 1389, pages 1319–1322. AIP, 2011.
- [14] O. Pironneau. On the transport-diffusion algorithm and its applications to the Navier-Stokes equations. *Numerische Mathematik*, 38(3):309–332, 1982.
- [15] J.-M. Qiu and G. Russo. A high order multi-dimensional characteristic tracing strategy for the Vlasov–Poisson system. *Journal of Scientific Computing*, 71(1):414–434, 2017.
- [16] J. Rossmannith and D. Seal. A positivity-preserving high-order semi-Lagrangian discontinuous Galerkin scheme for the Vlasov-Poisson equations. *Journal of Computational Physics*, 230:6203–6232, 2011.
- [17] J. Ryan, C.-W. Shu, and H. Atkins. Extension of a postprocessing technique for the discontinuous Galerkin method for hyperbolic equations with application to an aeroacoustic problem. *SIAM Journal on Scientific Computing*, 26(3):821–843, 2005.
- [18] M. M. Shoucri. A two-level implicit scheme for the numerical solution of the linearized vorticity equation. *International Journal for Numerical Methods in Engineering*, 17(10):1525–1538, 1981.
- [19] T. Xiong, J.-M. Qiu, Z. Xu, and A. Christlieb. High order maximum principle preserving semi-Lagrangian finite difference WENO schemes for the Vlasov equation. *Journal of Computational Physics*, 273:618–639, 2014.
- [20] X. Zhang and C.-W. Shu. On maximum-principle-satisfying high order schemes for scalar conservation laws. *Journal of Computational Physics*, 229:3091–3120, 2010.
- [21] H. Zhu, J. Qiu, and J.-M. Qiu. An h-adaptive RKDG method for the Vlasov–Poisson system. *Journal of Scientific Computing*, 69(3):1346–1365, 2016.

- [22] H. Zhu, J. Qiu, and J.-M. Qiu. An h-Adaptive RKDG Method for the Two-Dimensional Incompressible Euler Equations and the Guiding Center Vlasov Model. *Journal of Scientific Computing*, 73(2-3):1316–1337, 2017.